

X-ray diffraction
Advanced Laboratory Report
Faculty of Physics and Earth Sciences
Leipzig University

September 2022

Contents

1	Introduction	3
1.1	Basics of X-rays	3
1.1.1	Historical Overview	3
1.1.2	Generation of X-rays and X-ray Spectra	3
1.1.3	Nomenclature of Characteristic X-ray Lines	5
1.1.4	Moseley's Law	6
1.1.5	Absorption of X-rays	7
1.2	Crystal systems, derivation of Miller's indices	9
1.3	Relation of lattice spacing d and lattice constants for the 7 crystal systems	9
1.4	Derivation of Bragg-equation	9
1.5	Penetration Depth of X-Rays	10
1.6	Errors in goniometer measurement and methods for elimination of errors	11
1.7	Structure of polycrystalline samples and heteroepitaxial thin films	12
2	Task 1	14
2.1	Silicene	14
2.1.1	Miller's indices	14
2.1.2	Unit cell	16
2.1.3	Lattice parameters	16
2.2	ZnO	17
2.2.1	Miller's indices	17
2.2.2	Unit cell	19
2.2.3	Lattice parameters	20
3	Task 2	21
3.1	Task 2.1	21
3.1.1	Different peaks	21
3.2	Task 2.2	22
3.2.1	Peaks and FWHM	23
3.2.2	Lattice constants	24
3.2.3	FWHM discussion	24
4	Task 3	25
4.1	Diffraction pattern fit	25
4.2	Crystal structure of PbO	26
5	Summary	27

1 Introduction

The objective of this laboratory was to analyze the X-ray diffraction pattern of several powder substances and determine their nature as well as relevant crystal properties.

In the following section we include an excerpt of important theoretical concepts regarding the technique of X-ray diffraction before addressing the experimental tasks.

1.1 Basics of X-rays

1.1.1 Historical Overview

X-rays comprise the part of the electromagnetic spectrum that extends from wavelengths of about 10^{-9} m down to wavelengths of about $6 \cdot 10^{-12}$ m, or—equivalently—frequencies between $3 \cdot 10^{17}$ Hz and $5 \cdot 10^{19}$ Hz [1]. They were discovered in 1895, in Würzburg, by the German scientist Wilhelm Röntgen (an achievement that earned him the Nobel prize years later) while he experimented with discharge tubes, and hence the name in many languages—including the German *Röntgenstrahlung*. Röntgen did not know the physical origin of this kind of radiation, so he named it X-rays. Despite this initial ignorance, and as it is usually the trend in science, these newly found rays immediately acquired an importance that cannot be overstated. The X-rays allowed to see the internal structure of an opaque object when projected through it onto a photographic film; in the photograph, the "denser" materials will appear darker. This was the birth of *radiography*, and until today it has been massively used, especially in medicine and engineering.

The scale of applicability of radiography is however limited (down to a resolution of about $10 \cdot 10^3$ mm). In 1912, *X-ray diffraction* and the physical nature of X-rays were discovered, and with them, the capacity to inquire about the internal structure of a material down to a resolution of the order of 10^{-7} mm [3]. This laboratory is concerned with this application of X-ray technology.

1.1.2 Generation of X-rays and X-ray Spectra

Broadly, an X-ray generation device consists a tube where electrons are emitted from a heated cathode, accelerated by a voltage U , and impacted onto an anode. In the anode material (tungsten, for example) the electrons stop and part of their energy eU is converted into short wavelength (high energy) radiation—most of the energy is converted into heat and only close to 1% is converted into X-rays. These X-rays leave the tube through a window and can be further collimated with proper apertures [4]. X-ray tubes are in general divided into two types, that differ in the way in which electrons are produced: gas tubes, in which electrons are produced by the ionization of a small amount of gas; and filament tubes, in which the source of electrons is a hot filament (view Figure 1) [3].

X-rays are produced by two different effects, which give rise to two different spectra:

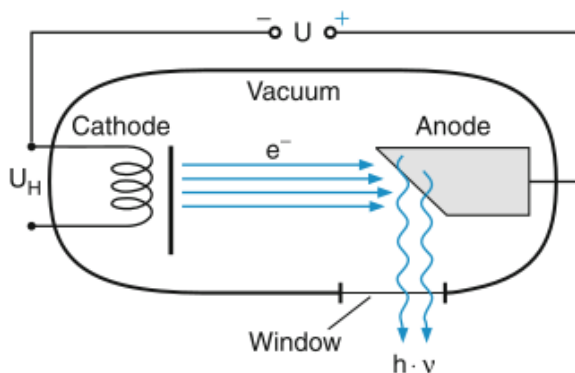


Figure 1: Schematic illustration of an X-ray tube [4].

1. By decelerating energetic electrons (or any charged particle to be more precise) —with energies ranging from keV to MeV—that give rise to the *Bremsstrahlung*, also known as *braking radiation* or *white radiation*. This is the *continuous spectrum*.
2. The energetic electrons exciting inner shell electrons on transitions to a higher non occupied state of the atoms of the anode E_i . The higher energy states E_n emit X-rays as spectral lines in transitions $E_n \rightarrow E_k$ back down to the state E_k , with wavelength λ_{nk} characteristic of the anode material. Therefore, this X-rays are called *characteristic spectrum*.

In the case of Bremsstrahlung, the continuous spectrum arises from the fact that though (according to the laws of electrodynamics) every decelerated charge emits energy, not all the electrons in an X-ray device decelerate in the same way: some stop completely in one impact and release all their energy at once, while others are deflected here and there by the atoms of the target, losing fractions of their energy until it is all spent (Figure 2). This process clearly creates a radiation continuum with a high energy limit given by those electrons who stop completely upon impact and that have a kinetic energy $E_{kin} = eU = h\nu_{max}$. Furthermore, this gives the condition

$$h\nu \leq h\nu_{max} = eU \Rightarrow \lambda \geq \lambda_{min} = \frac{hc}{eU} \quad (1)$$

where λ_{min} is known as the *short-wavelength limit*, and is the wavelength value at which the intensity ceases to be zero. The intensity of the Bremsstrahlung can be increased using heavy elements (such as tungsten) or increasing the current (and hence the number of electrons per second striking the target), but the short-wavelength limit and the wavelength distribution are functions of the voltage only (as can be seen in Equation 1).

On the contrary, the characteristic spectrum has wavelengths that will only depend on the element and the

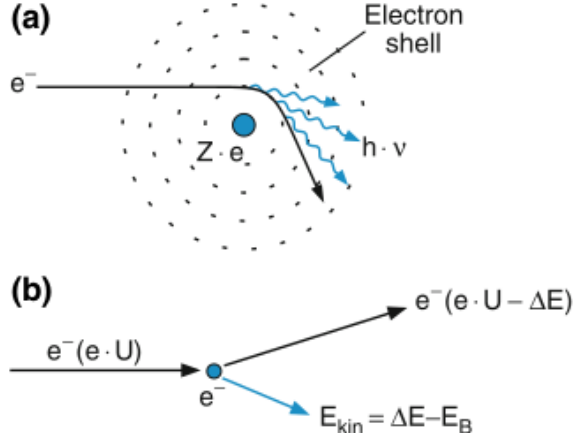
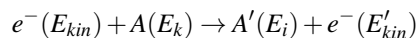
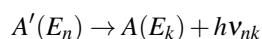


Figure 2: Origin of Bremsstrahlung. (a) Deceleration in a Coulomb potential. (b) Inelastic scattering [4].

transition energies between energy levels. It is so because when the incident electron e^- (with energy E_{kin}) excite inner shell electrons in the atom A (with energy E_k) to a higher unoccupied state (with energy E_i), it creates an inner shell vacancy. This vacancy will be filled with an electron from a higher energy level (E_n) and emit the excess energy as X-radiation of energy $h\nu_{nk}$, according to the following scheme

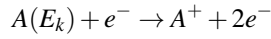


with $E_{kin} - E'_{kin} = E_i - E_k$. And to fill the vacancy



with $h\nu_{nk} = E_n - E_k$.

The energy difference between the state E_n and the state E_k is what determines the peak in the characteristic spectrum, and E_n can be many higher energy states, including E_i ; that is what creates the whole characteristic spectrum when many atoms are considered [4]. It is noteworthy mentioning that the energy of the impacting electron could be so big that the inner shell electron is kicked off the atom, to a scattering state, ionizing the atom. In that case, the scheme of the interaction would be



Regardless, the characteristic spectrum is composed of sharp intensity maxima at certain wavelengths superimposed on the continuous spectrum (see Figure 3). These characteristic lines only appear past a given critical voltage, since they are otherwise absorbed into the Bremsstrahlung.

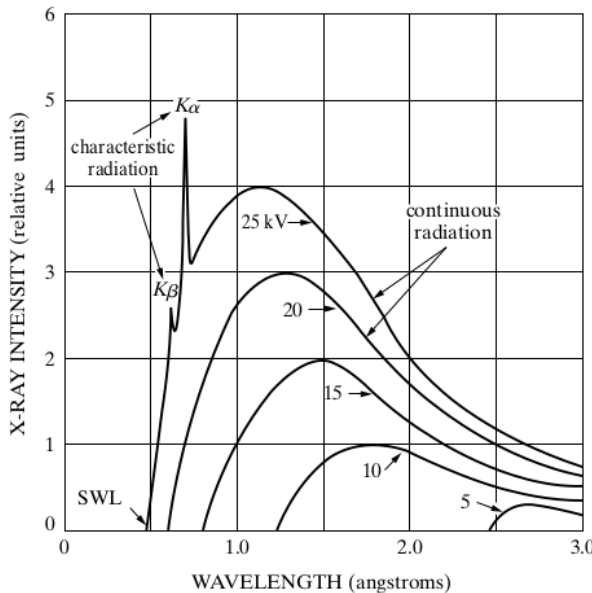


Figure 3: Characteristic spectrum of molybdenum as a function of applied voltage. Notice that the characteristic peaks only appear after a critical voltage value [3].

1.1.3 Nomenclature of Characteristic X-ray Lines

The characteristic lines are classified as K, L, M, \dots , in order of increasing wavelength (decreasing energy), and each Latin letter corresponds to the principal quantum number $n = 1, 2, 3, \dots$. Usually only the K lines are useful in X-ray diffraction, since the rest are too easily absorbed.

The K line set is further divided into several lines, although normally only the three strongest are seen in diffraction work: K_{α_1} , K_{α_2} , and K_{β} (Figure 4). The $K_{\alpha_{1,2}}$ correspond to the energy emitted from a $L \rightarrow K$ transition and the K_{β} from a $M \rightarrow K$ transition. The subdivisions of the K_{α} are due to fine structure (spin-orbit coupling); considering the selection rules for optical transitions, $\Delta l = \pm 1$ and $\Delta j = 0, \pm 1$, the lines K_{α_1} and K_{α_2} correspond to the transitions from the states $n = 2^2 P_{1/2}$ and $n = 2^2 P_{3/2}$ to the state $n = 1^2 S_{1/2}$, respectively, in a manner analogous to with the notorious sodium D lines [5]. The wavelengths of the K_{α_1} and K_{α_2} are so similar that they are not always resolved; if resolved, they are called K_{α} doublet and, if not, they are just called K_{α} line. To be more precise, the K_{β} line presents also fine-structure splitting, but that is also usually even harder to resolve.

Considering the nature of these transitions, it follows naturally that the K_{α} line is always the strongest line in an X-ray spectrum of an element.

Of particular relevance is mentioning that it is the existence of the strong K_{α} line what in general makes the X-ray

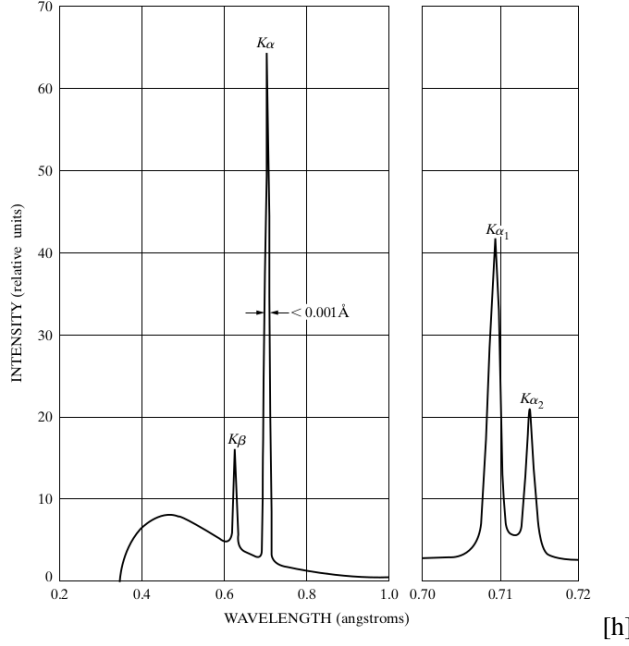


Figure 4: Spectrum of molybdenum at 35 kV. Line widths not to scale. Resolved K_α doublet is shown on an expanded wavelength scale at the right [3].

diffraction experiments possible, because many of them require approximately monochromatic radiation. For this reason, it is necessary the usage of filters to reduce the undesirable components of the radiation, be it the white noise or the K_β peak. To achieve this, filters made out of materials with a K absorption edge between the K_α and K_β peaks are used. This filtering is never perfect, but, for most purposes, a reduction of 1/500 in the intensity ratio K_α/K_β is sufficient.

This notation for the spectral lines is known as *Siegbahn notation* and is customarily used in X-ray spectroscopy over more precise notations, such as term symbol notation. Most of the characteristic lines of known elements have been tabulated, mainly in Siegbahn's work, and it has allowed to evidence that, for example, not all the L lines are what is considered traditionally as "low energy", but that it depends on the element. For example, an L_{α_1} line of a heavy element, like tungsten, can have roughly the same energy of a K_{α_1} line of a lighter element, like copper.

1.1.4 Moseley's Law

Henry G.J. Moseley found in 1913 that the wavelength of any any characteristic line increased with the atomic number of the emitter element (Figure 5). This is formalized in what became known as *Moseley's law*

$$\sqrt{v} = C(Z - \sigma) \quad (2)$$

with C and σ constants.

The functional form of this law is immediately relatable to the contemporary Bohr-Sommerfeld atomic model. As a matter of fact, that was indeed the rationale with which Moseley tried to justify the linear fit $\sqrt{v} \propto Z$ [9]. The law can be rewritten in a way in which this is more evident

$$\frac{1}{\lambda} = R_H \cdot (Z - \sigma)^2 \cdot \left(\frac{1}{n_1^2} - \frac{1}{n_2^2} \right) \quad (3)$$

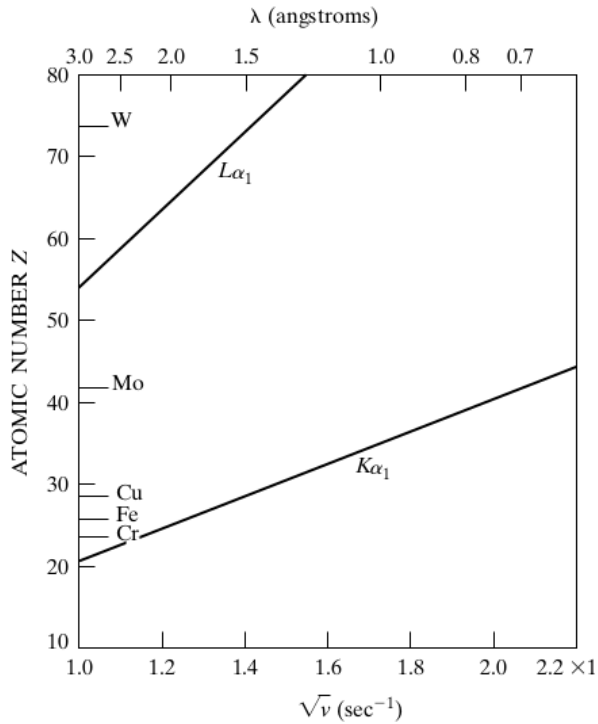


Figure 5: Moseley's law between \sqrt{v} and Z for two characteristic lines [3].

However, [Equation 3](#) is just a very useful approximation. A more formal approach using the *central field approximation* for the frequency of the K_α lines would be

$$v_{K\alpha} = \frac{(Z - \sigma_{10})^2}{1^2} - \frac{(Z - \sigma_{21})^2}{2^2} \quad (4)$$

where σ_{nl} are the screening factors for the respective energy levels, and n and l are the usual quantum numbers. Moseley's approximation assumes $\sigma = \sigma_{10} = \sigma_{21}$, which is a good approximation (for $12 \leq Z \leq 41$), but we should not overlook that it is still an empirical law. (For more detail about this topic see [10]).

1.1.5 Absorption of X-rays

When X-rays encounter matter they are partially transmitted and partially absorbed. Röntgen determined that the fractional decrease in intensity I while passing through a homogeneous material is proportional to the distance traveled [3], i. e.

$$-\frac{dI}{I} = \mu dx$$

with solution

$$I_x = I_0 e^{-\mu x} \quad (5)$$

where μ is called *linear absorption coefficient*, and it is proportional to the density of the substance ρ , so it is the quotient $\frac{\mu}{\rho}$, which allows to rewrite equation [Equation 5](#) one in the form

$$I_x = I_0 e^{(\mu/\rho)\rho x} \quad (6)$$

If the substance is not homogeneous, [Equation 6](#) has to be modified by considering a properly weighted linear function.

The analysis of the variation of the quantity μ/ρ gives valuable information about how the X-rays interact with atoms. The typical curve of μ/ρ vs wavelength shows characteristic curves, called *branches*, that are separated by very sharp discontinuities (see [Figure 6](#)). This is due to the fact that the main source of loss of intensity of the incoming beam is not scattering (random loss of intensity), but rather *true absorption*, which is caused by electronic transitions inside the atoms of the substance. In a completely analogous manner to an incident energetic electron, an X-ray quantum of enough energy can knock off an inner shell electron, case in which the incoming energy is transformed into the kinetic energy of the ejected photoelectron and *fluorescent radiation* emitted equal to the energy difference between the original energy level and the level from which the atom relaxes back. It is easy to understand the shape of the graph in [Figure 6](#) once one considers that increasing frequency opens new channels of absorption every time that a critical value is reached, corresponding to the minimum energy to create a given vacancy. The absorption profile will not only show the peaks corresponding to every critical energy value, but also the fine structure of each level in the form of small peaks.

Empirical results show that, along each branch of absorption, the quantity μ/ρ varies with wavelength as

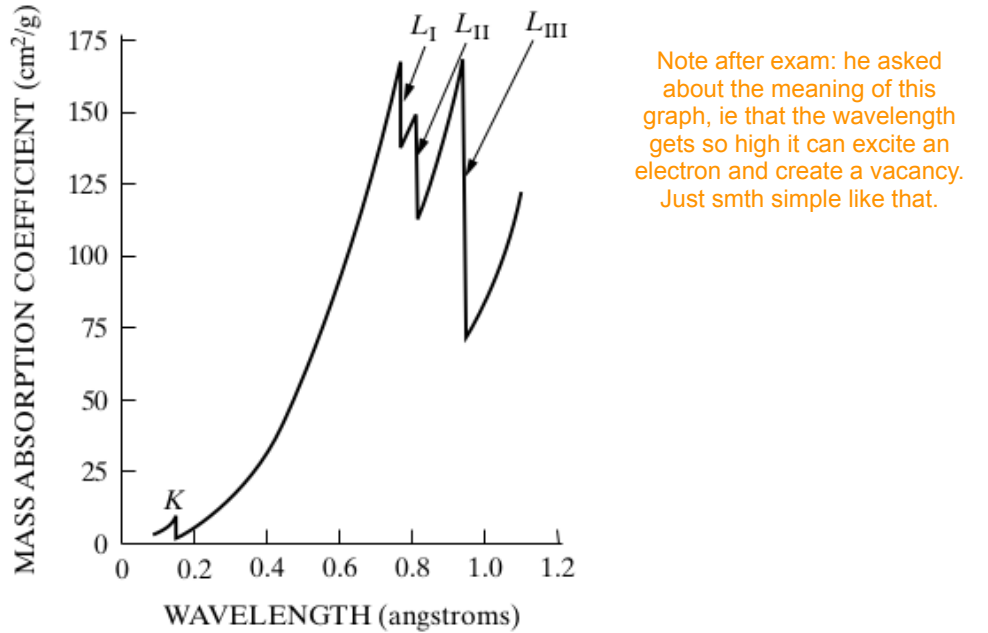


Figure 6: Absorption coefficients of lead, showing *K* and *L* absorption edges [3].

$$\frac{\mu}{\rho} = k\lambda^2 Z^3 \quad (7)$$

where k is a constant [3].

From [Equation 7](#) is clear that the more energetic X-rays, named accordingly *hard*, are more penetrating (or less absorbed).

Finally, it is important to consider that not every time that an X-ray is quantum is absorbed, creating a vacancy in the *K* shell, *K* radiation is produced. It is also possible to expel this excess energy with the ejection of an outer shell electron with exactly that kinetic energy. This phenomenon is known as the *Auger effect* and for light atoms ($Z < 31$) it is the predominant effect over fluorescence.

1.2 Crystal systems, derivation of Miller's indices

The following (chapters 1.2 to 1.4) is the summary of the theoretical background necessary for the experiments, based on “Fortgeschrittenen-Praktikum High-Resolution X-Ray Diffraction“ by Walter-Schottky-Institut und TU München, September 2007.

1.3 Relation of lattice spacing d and lattice constants for the 7 crystal systems

The reciprocal lattice vector

Note after exam: he asked us what Miller's indices are.

$$\vec{G}_{hkl} = h\vec{b}_1 + k\vec{b}_2 + l\vec{b}_3 \quad (8)$$

is perpendicular to the lattice planes with Miller indices (hkl) and the distance d_{hkl} between two such adjacent planes is given by

$$2d_{hkl} = \frac{2\pi}{|\vec{G}_{hkl}|} \quad (9)$$

Depending on the crystal structure, the dependence on lattice parameters can take various forms which can be seen on Figure 7.

<i>Cubic:</i>	$\frac{1}{d^2} = \frac{h^2 + k^2 + l^2}{a^2}$
<i>Tetragonal:</i>	$\frac{1}{d^2} = \frac{h^2 + k^2}{a^2} + \frac{l^2}{c^2}$
<i>Hexagonal:</i>	$\frac{1}{d^2} = \frac{4}{3} \left(\frac{h^2 + hk + k^2}{a^2} \right) + \frac{l^2}{c^2}$
 <i>Rhombohedral:</i>	
$\frac{1}{d^2} = \frac{(h^2 + k^2 + l^2)\sin^2\alpha + 2(hk + kl + hl)\cos^2\alpha - \cos\alpha}{a^2(1 - 3\cos^2\alpha + 2\cos^3\alpha)}$	
<i>Orthorhombic:</i>	$\frac{1}{d^2} = \frac{h^2}{a^2} + \frac{k^2}{b^2} + \frac{l^2}{c^2}$
<i>Monoclinic:</i>	$\frac{1}{d^2} = \frac{1}{\sin^2\beta} \left(\frac{h^2}{a^2} + \frac{k^2\sin^2\beta}{b^2} + \frac{l^2}{c^2} - \frac{2hl\cos\beta}{ac} \right)$
<i>Triclinic:</i>	$\frac{1}{d^2} = \frac{1}{V^2}(S_{11}h^2 + S_{22}k^2 + S_{33}l^2 + 2S_{12}hk + 2S_{23}kl + 2S_{13}hl)$

Figure 7: Formulas to calculate lattice spacing for different lattice structures [3]

1.4 Derivation of Bragg-equation

We define the scattering vector to be the difference between the incident and scattering beam.

$$\vec{q} = |\vec{k}_{out}| - |\vec{k}_{in}| \quad (10)$$

We consider the scattering to be an elastic process, so the scattered wave exhibits the same frequency and the same norm of the wave vector as the incident wave.

$$|\vec{k}_{out}| = |\vec{k}_{in}| = |\vec{k}| = \frac{2\pi}{\lambda} \quad (11)$$

Thus the maximum length of the scattering vector in case of backscattering ($\theta = 90^\circ$, see Figure 8) is

$$q = 2|\vec{k}| = \frac{4\pi}{\lambda} \quad (12)$$

Only if the scattering vector is equal to a reciprocal lattice vector, an X-ray reflex can be observed,

$$\vec{q} = \vec{G} \quad (13)$$

because then the scattered X-rays interfere constructively along the direction of \vec{k}_{out} , that is to say the phase factors of the waves scattered at different lattice points of the crystal differ only by a factor $e^{2i\pi n}$ (with n integer) along \vec{k}_{out} . If the phase factor has a slightly different value than $e^{2i\pi n}$, the contribution from the all lattice points average to zero very effectively due to the high number of scatterers. The intensity for the observed X-ray reflex is then proportional to V^2 , and thus to N^2 , where N is the number of lattice points. Combining the Laue condition and the equation for the distance between two adjacent planes, we obtain the Bragg equation

$$2d_{hkl} \sin \theta = n\lambda \quad (14)$$

where θ is the angle between the incoming angle and the planes (Figure 8). The diffraction condition then amounts to the requirement that the path difference for waves reflected by adjacent lattice planes has to be an integer multiple of the wave length λ . The Bragg equation relates every X-ray reflex that can be observed with a set of parallel lattice planes (hkl) (the scattering vector has to be equal to a reciprocal lattice vector). The Laue condition, however, assigns every X-ray reflex to a reciprocal lattice point which make it convenient to label the reflexes with the indices of their corresponding reciprocal lattice points HKL . All such points make up a hemisphere with radius equal to $\frac{4\pi}{\lambda}$, the maximum value of the scattering vector. We call this the Ewald sphere (Figure 8).

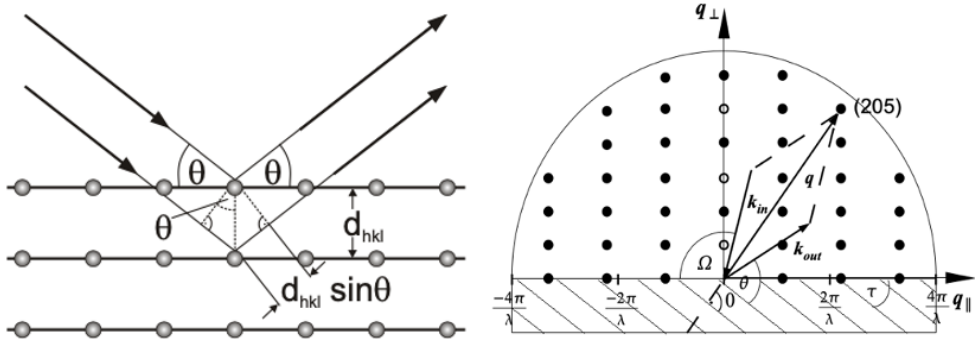


Figure 8: Left: A scheme of the Bragg equation. Right: The Ewald sphere (reciprocal lattice points) [6]

1.5 Penetration Depth of X-Rays

The energetic X-rays penetrate in the specimen and is absorbed, reflected at the planes of the crystal structure, and passes through the material again. The absorption fraction $A(t)$ is dependent on the penetration x , the incidence angle ω , and the diffraction angle θ [12]. For different materials it is expressed through the linear absorption coefficient μ and has the form

$$A(x) = 1 - e^{-\mu x} \left(\frac{1}{\sin \omega} + \frac{1}{\sin(2\theta - \omega)} \right) \quad (15)$$

Knowing μ for a given material and solving for x gives the given absorption at a given depth.

The penetration depth d (or δ) is then defined as the percentual fraction $1 - 1/e \approx 63\%$ of the absorption —or,

equivalently, the depth x at which the intensity of the radiation inside the material falls to $1/e \approx 37\%$ of the original value, which renders

$$d = \frac{1}{\mu \left(\frac{1}{\sin \omega} + \frac{1}{\sin(2\theta - \omega)} \right)} \quad (16)$$

The penetration depth should always be considered within the experimental setup since some material and radiation combinations entail a very bad penetration, such as iron (or iron alloys) with copper radiation. In Figure 9 we have some typical penetration depth values for different elements and types of radiation.

Z	ρ [gcm ⁻³]	Co-Strahlung		Cu-Strahlung		Mo-Strahlung	
		$\omega = 1^\circ$	$\omega = 15^\circ$	$\omega = 1^\circ$	$\omega = 15^\circ$	$\omega = 1^\circ$	$\omega = 15^\circ$
C	6	2,27	9,64	17,37	15,35	117,9	169,2
Al	13	2,70	0,83	6,38	1,29	9,91	12,70
Si	14	2,33	0,77	5,95	1,20	9,23	11,75
Fe	26	7,86	0,38	2,89	0,067	0,52	0,58
Cu	29	8,92	0,24	1,88	0,37	2,82	0,39
Zn	30	7,14	0,28	2,13	0,42	3,21	0,45
Zr	40	6,51	0,12	0,99	0,19	1,48	1,60
W	74	19,25	0,035	0,27	0,052	0,40	0,092
							0,70

Note after exam: he asked us the approximate penetration depth, which can be seen from this table. It basically has to be a bit longer than the thin film thickness for this XRD method, so we see both thin film and substrate (and get somewhat similar intensities for both).

Figure 9: Penetration depth of several elements (in μm) for an absorption of 63%, a diffraction angle of $\theta = 15^\circ$, and different incidence angles ω and types of radiation [12].

1.6 Errors in goniometer measurement and methods for elimination of errors

In our experiment, the measurements for the diffraction peaks are made through a commercial diffractometer. For the case of a diffractometer, the sources of systematic error in d are:

- Misalignment of the instrument
- Use of a non-flat specimen
- Absorption in the specimen
- Displacement of the specimen from the diffractometer axis (the largest source of error)
- Vertical divergence of the incident beam

Methods to eliminate include carefully following the instructions manual to align the components and adjusting the specimen surface to coincide as closely as possible with the diffractometer axis. The evaluation of the θ value is in the sinus function, such that the change in θ is close to $\pi/2$ and would become negligible. An extrapolation can be applied to decrease the measurement error for cubical structure with the following equation:

$$\frac{\delta d}{d} = \frac{\delta}{a} = \frac{a - a_0}{a} = -\cot \theta \delta \theta \quad (17)$$

or using the Nelson-Riley function

$$\frac{\delta}{a} = \frac{1}{2} \left(\frac{\cos^2 \theta}{\sin \theta} + \frac{\cos^2 \theta}{\theta} \right) \quad (18)$$

For obtaining the best value of parameter a , the measured values are plotted to the fit function, such that the value at the y -axis would become the least uncertain final value; due to the fact that the uncertainty expression reduces to zero with the fitted function.

1.7 Structure of polycrystalline samples and heteroepitaxial thin films

In real crystals, the requirement to minimize the free energy $F = U - TS$ induces deviations from the ideal crystal structure. Drastic changes can be seen already by small concentrations of defects. For example the electrical conductivity of a semiconductor can be significantly increased by the incorporation of a small amount of extrinsic impurities which is known as doping. Therefore it is important to investigate the nature and density of defects. We use High- Resolution X-Ray Diffraction (HRXRD) as it does not damage the film and the preparation of the sample is simple. We use heteroepitaxially grown thin films. Homoepitaxial means that the substrate and epitaxial layer are of the same material, heteroepitaxial implies that they are different. Therefore there is typically also a mismatch between lattice constants and perhaps even crystal symmetry. The lattice mismatch can be described by

$$\frac{\Delta a}{a} = \frac{a_{\text{substrate}} - a_{\text{film}}^{\text{relaxed}}}{a_{\text{substrate}}} \quad (19)$$

where $a_{\text{substrate}}$ and $a_{\text{film}}^{\text{relaxed}}$ are the relaxed lattice constants.

For a small lattice mismatch the epitaxial film can grow pseudomorphical, i.e. it adapts the in-plane lattice constant of the substrate thereby accumulating biaxial strain.

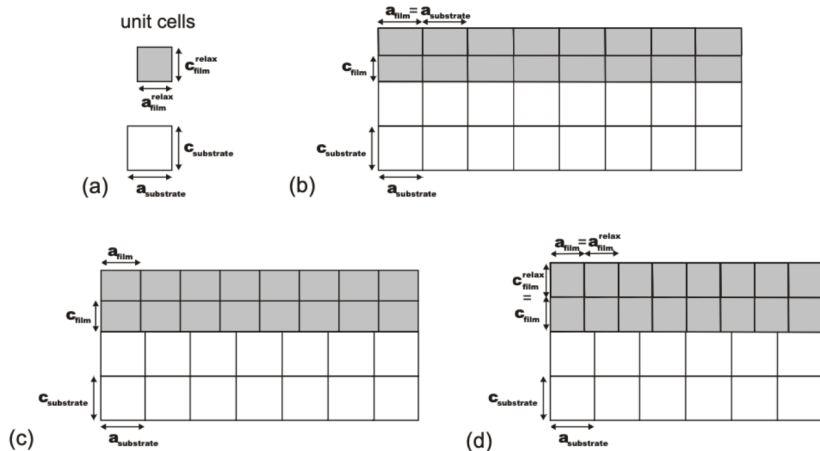


Figure 10: Schemes of possible effects of lattice mismatch. (a) Relaxed unit cells of film and substrate, (b) a pseudomorphical (c) a partially relaxed and (d) a fully relaxed heteroepitaxial film [6]

When the film thickness exceeds a certain critical value, the built-up strain energy is released by the formation of one-dimensional defects, called dislocations, perpendicular to the interface. In the vicinity of a dislocation the crystal lattice is distorted and strain is accumulated, that decays rather slowly as one moves away from the dislocation. By moving along a 360°-loop around a dislocation, one does not arrive at one's starting point. The difference between the starting and end point defines the Burger vector \vec{B} .

The dislocations can be generally categorised to two groups: namely screw-type and edge-type dislocations (Figure 11). The Burgers vector is oriented along the dislocation for the screw-type and perpendicular to the dislocation for the edge-type. To minimise the energy, dislocations have the tendency to arrange themselves in the stablest configuration possible, for example the edge-type dislocations prefer to group together (Figure 11). Such an agglomeration of dislocations is known as grain boundary. This type of two-dimensional defect can be seen as a boundary between two monocrystalline regions of a solid, called crystallites, which are twisted by an angle $\delta\Omega$ with respect to one another. In a similar way as edge-type dislocations result in a twist, screw-type dislocations can give rise to a tilt of the crystallites.

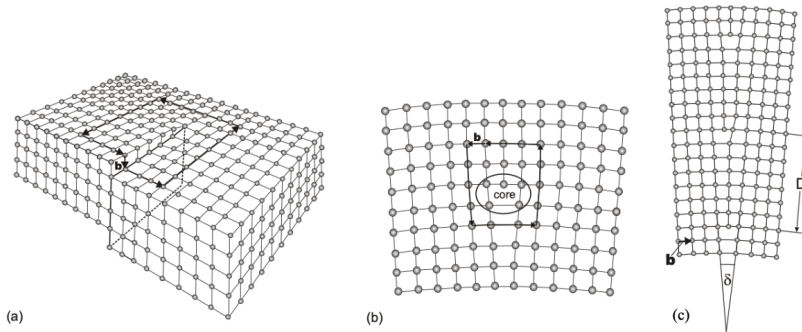


Figure 11: a) screw-type dislocation b) edge-type dislocation c) grain boundary [6]

2 Task 1

We measure measure with the Philips X'Pert diffractometer in Bragg-Brentano geometry the X-ray diffraction patterns (2θ - ω scan) of two polycrystalline bulk samples for 2θ angles from 20° to 120° (Si, Al) and 20° to 100° (ZnO) with step size 0.02° , and measuring time 0.5 sec. per step. Using the X'Pert High Score software, a list of all peaks can be generated without and with deconvolution of the K_{α_1} / K_{α_2} peaks. From the graphs we derive the Miller's indices (hkl) by comparison with suitable patterns from the PC-PDF data base. Secondly, we show and discuss by means of a scheme in the protocol the unit cells and calculate the lattice spacing d of all peaks the lattice constants. We then perform error correction of the lattice parameters by extrapolation using different functions

2.1 Silicone

Our first sample is a powdered silicone.

2.1.1 Miller's indices

The graphs obtained from X-ray diffraction patterns is shown below (figures 13 and 14). The Miller's indices assigned to the peaks were taken from comparing with the database (Figure 12.) Comparing the measured and theoretical two we can see that the angles correspond quite well in between the two.

Figure 12: Screenshot of the database for Si. We choose one that covers all the angles we need.

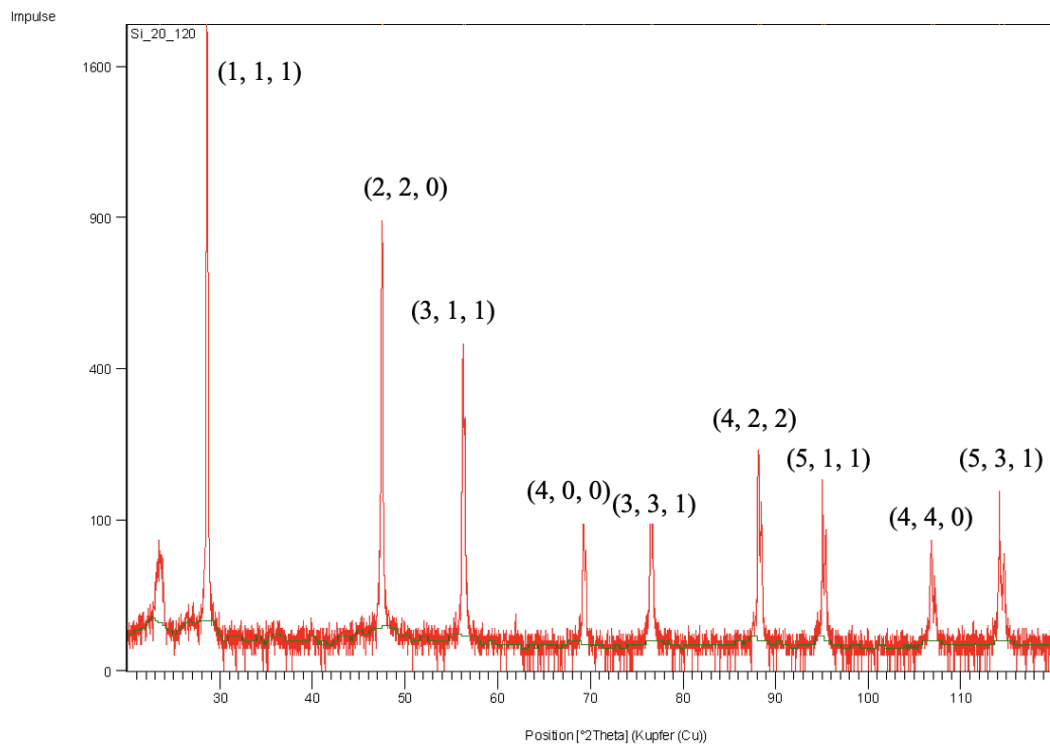


Figure 13: Measured 2θ vs intensity spectrum

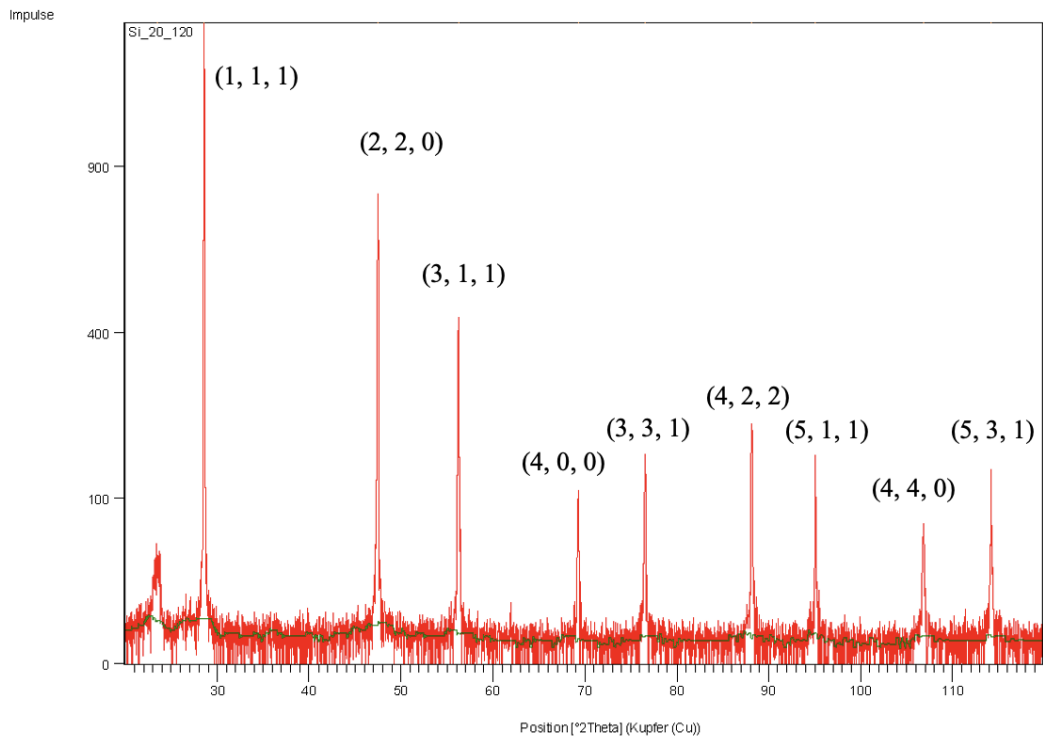


Figure 14: Measured 2θ vs intensity spectrum with deconvolution of the $K_{\alpha_1} / K_{\alpha_2}$

Using the X'Pert High Score software we can generate a list of exact peak locations and the corresponding d values (Figure 15). From the latter later lattice parameters can be calculated.

2θ	Peak height [cts]	d [Å]	Indices	2θ	Peak height [cts]	d [Å]	Indices
28.6204	1824.60	3.11904	111	28.5962	1216.40	3.11904	111
47.4643	880.01	1.91397	220	47.4643	586.67	1.91397	220
56.2809	462.83	1.63325	311	56.2809	308.56	1.63325	311
69.2928	98.76	1.35494	400	69.2928	65.84	1.35494	400
76.5330	139.02	1.24378	331	76.5330	92.68	1.24378	331
88.1859	20.79	1.10703	422	88.1859	139.86	1.10703	422
95.1331	111.53	1.04368	511	95.1331	74.35	1.04368	511
106.8664	68.52	0.95908	440	106.8664	45.68	0.95908	440
114.2508	13.87	0.91717	531	114.2508	92.58	0.91717	531

Figure 15: Table with peak list and values for d with assigned Miller's indices, just as is on the left and with deconvolution of the $K_{\alpha_1}/K_{\alpha_2}$ on the right

2.1.2 Unit cell

The silicon crystal has an face-centered cubic (FCC) structure and has one lattice parameter a . This can be calculated using the Bragg equation.

The silicone crystal has 8 atoms at corners at 1/8 each in cell, 6 atoms in faces at 1/2 each in cell, and 4 atoms within cell. Thus total of 8 Si atoms per unit cell [13].

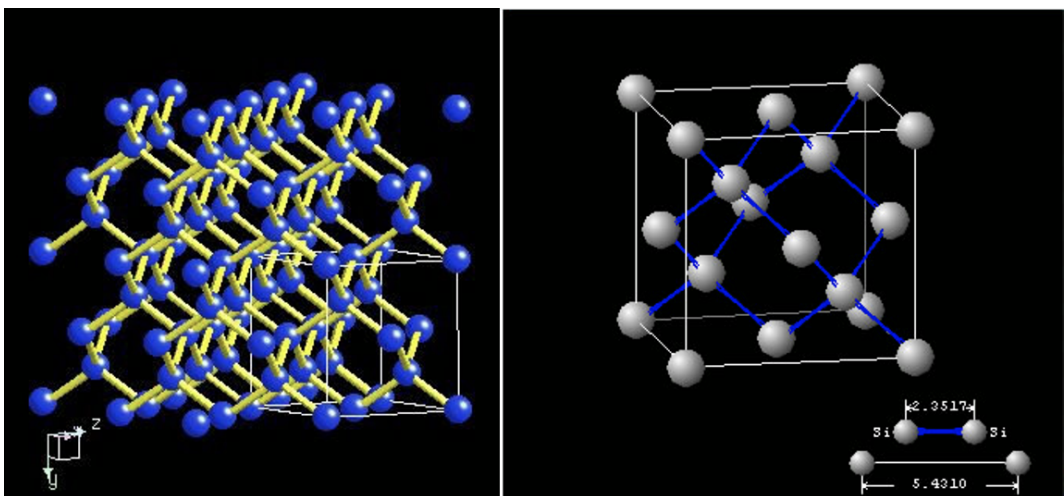


Figure 16: Si unit cell [13]

2.1.3 Lattice parameters

Combining equations (8) and (9) for a cubic lattice we obtain

$$a = \frac{\lambda \sqrt{h^2 + k^2 + l^2}}{2 \sin \theta}$$

Using $\lambda=1.5406 \text{ \AA}$ from literature, we obtain the following a values (Figure 17)

2θ	Indices	$a [\text{\AA}]$
28.6204	111	5.398
47.4643	220	5.414
56.2809	311	5.416
69.2928	400	5.420
76.5330	331	5.422
88.1859	422	5.423
95.1331	511	5.423
106.8664	440	5.425
114.2508	531	5.426

Figure 17: Si lattice parameter a

These a values are plotted against functions of θ corresponding to different error variations (Figures 18- 20), and the y -intercept is the a at 90° . The Nelson-Riley function is the most suitable for fitting and gives us a lattice constant

$$a = 5.432 \text{ \AA} \quad (20)$$

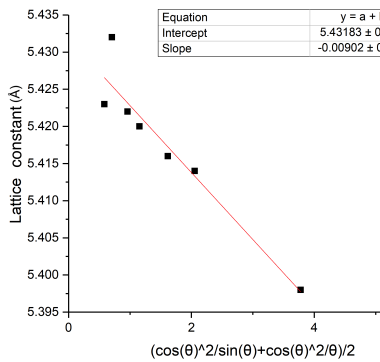


Figure 18: Nelson-Riley function

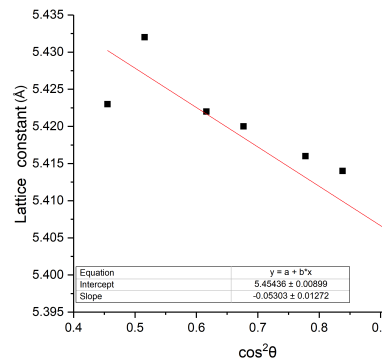


Figure 19: $\cos^2\theta$

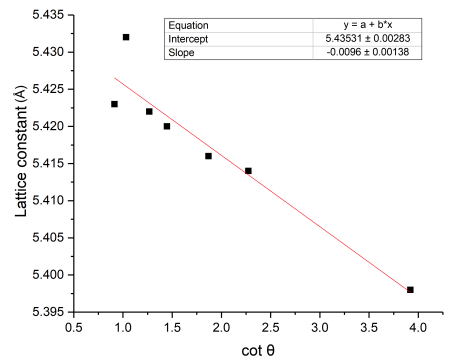


Figure 20: $\cot\theta$

2.2 ZnO

Our second sample is powdered ZnO.

2.2.1 Miller's indices

The graphs obtained from X-ray diffraction patterns is shown below (figures 22 and 23). The Miller's indices assigned to the peaks were taken from comparing with the database (Figure 21).

80-0075		Wavelength= 1.54060						
ZnO		2 θ	Int	h	k			
Zinc Oxide		31.728	578	1	0 0			
		34.40	442	0	0 2			
		36.212	999*	1	0 1			
		47.494	229	1	0 2			
		56.519	324	1	1 0			
		62.803	276	1	0 3			
Rad.: CuK α 1 λ : 1.54060 Filter:	d-sp: Calculated	66.283	44	2	0 0			
Cut off: 17.7 Int.: Calculated I/Icor.: 5.43		67.866	243	1	1 2			
Ref: Calculated from ICSD using POWD-12++, (1997)		68.992	114	2	0 1			
Ref: Garcia-Martinez, O et al., Solid State Ionics, 63, 442 (1993)		72.516	19	0	0 4			
Sys.: Hexagonal S.G.: P6 3 mc (186)		76.860	38	2	0 2			
a: 3.2539(1) b: 5.2098(3) c: 5.2098(3)	A: 1.6011	81.315	19	1	0 4			
α :	β :	γ :	Z: 2	mp:	89.50	74	2	0 3
Ref: Ibid.								
Dx: 5.658	Dm:	ICSD # : 067849						
Peak height intensity. R-factor: 0.000. PSC: hP4. Mwt: 81.38. Volume[CD]: 47.77.								
 © 1998 JCPDS—International Centre for Diffraction Data. All rights reserved PCPDFWIN v. 2.00								

Figure 21: Screenshot of the database for Si. We choose one that covers all the angles we need.

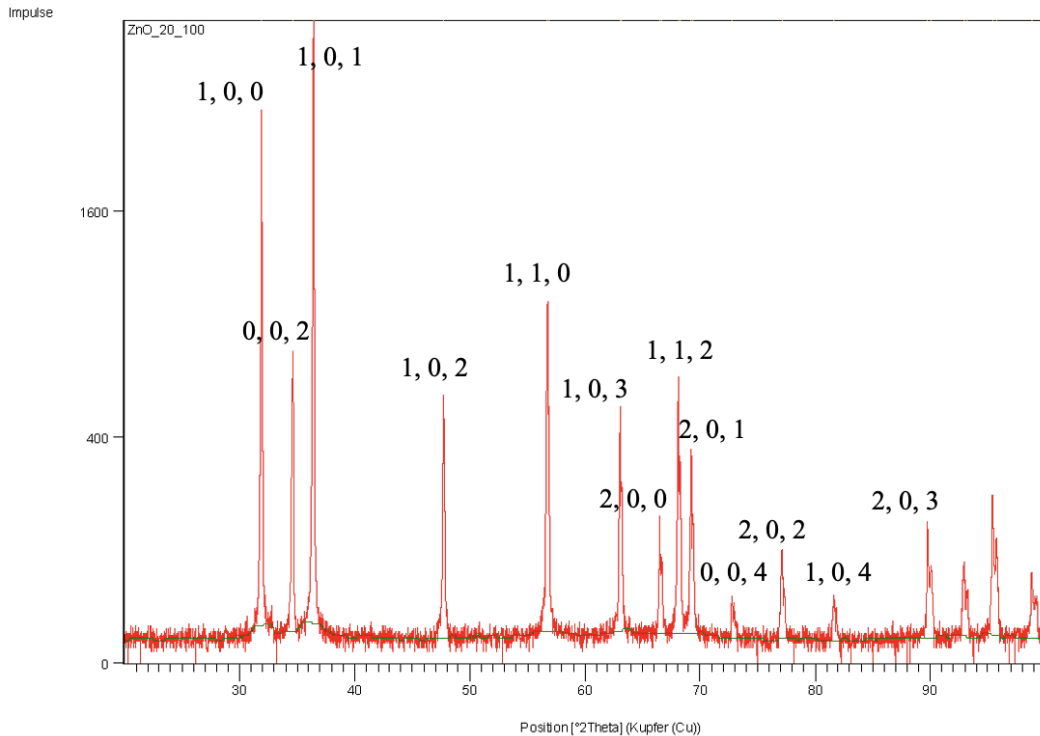


Figure 22: Measured 2 θ vs intensity spectrum

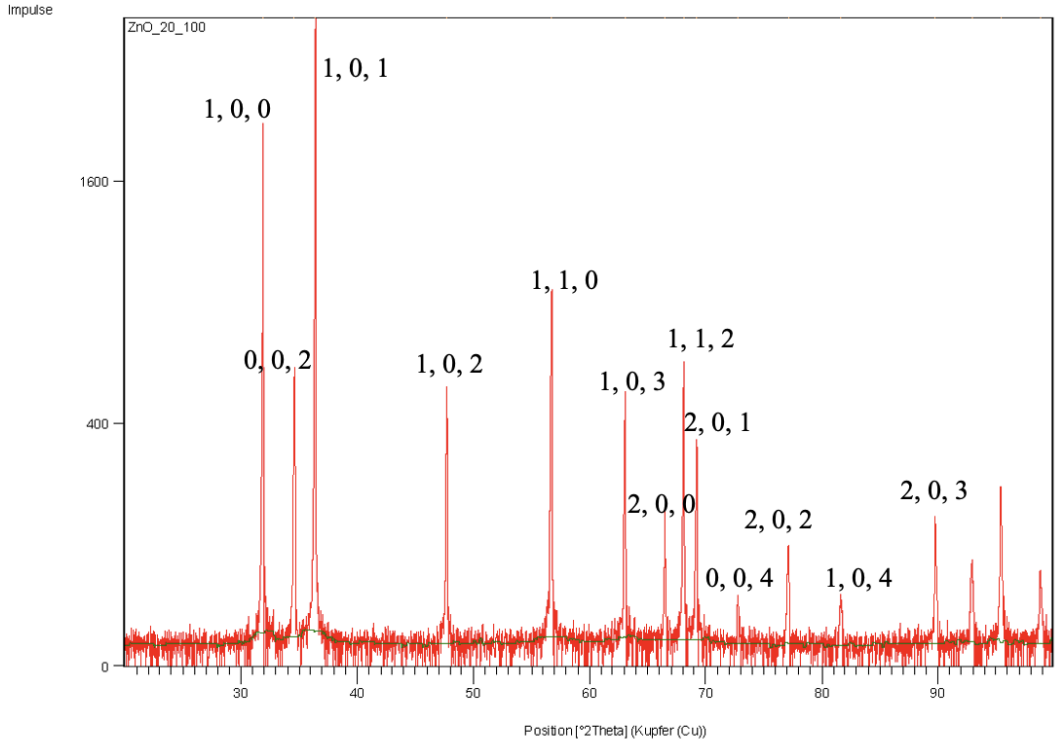


Figure 23: Measured 2θ vs intensity spectrum with deconvolution of the $K_{\alpha_1} / K_{\alpha_2}$

Using the X’Pert High Score software we can generate a list of exact peak locations and the corresponding d values (Figure 24). From the latter later lattice parameters can be calculated.

2θ	Peak height [cts]	d [\AA]	Indices	2θ	Peak height [cts]	d [\AA]	Indices
31.8991	2390.33	2.80554	100	31.8720	1593.56	2.80554	100
34.5872	708.08	2.59340	002	34.5577	472.05	2.59340	002
36.3938	3275.87	2.46871	101	36.3626	2183.91	2.46871	101
47.6898	539.52	1.90702	102	47.6479	359.68	1.90702	102
56.7247	975.22	1.62153	110	56.7247	650.15	1.62153	110
63.0464	51.04	1.47329	103	63.0464	340.70	1.47329	103
66.5014	162.00	1.40488	200	66.5014	108.00	1.40488	200
68.1048	631.91	1.37566	122	68.1048	421.27	1.37566	122
69.2209	348.39	1.35617	201	69.2209	232.26	1.35617	201
72.7693	23.05	1.29854	004	72.7693	15.37	1.29854	004
77.1014	96.04	1.23602	202	77.1014	64.03	1.23602	202
81.6267	27.44	1.17855	104	81.6267	18.29	1.17855	104
89.7880	133.69	1.09139	203	89.7880	89.13	1.09139	203

Figure 24: Table with peak list and values for d with assigned Miller’s indices, just as is on the left and with deconvolution of the $K_{\alpha_1} / K_{\alpha_2}$ on the right

2.2.2 Unit cell

The crystal structures shared by ZnO are wurtzite, zinc blende, and rocksalt as schematically shown in Figure 25. Under ambient conditions, the thermodynamically stable phase is that of wurtzite symmetry. The zinc blende ZnO structure can be stabilized only by growth on cubic substrates, and the rocksalt structure may be obtained at relatively high pressures. The wurtzite structure has a hexagonal unit cell with two lattice parameters a and c , in aratio of $\frac{c}{a} = \sqrt{\frac{8}{3}}$ (in an ideal wurtzite structure) [11].

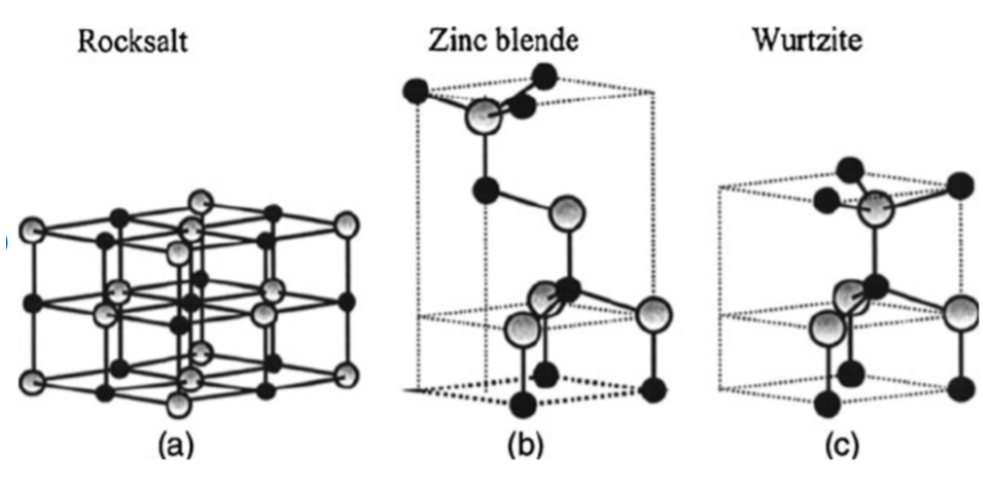


Figure 25: ZnO unit cell [11]

2.2.3 Lattice parameters

Combining equations (8) and (9) for a hexagonal structure we obtain

$$\frac{n\lambda}{2\sin\theta} = \frac{a}{\sqrt{\frac{4}{3}(h^2 + k^2 + hk) + (\frac{a}{c})^2 l^2}}$$

Considering $h=k=0$ this becomes

$$\frac{n\lambda}{2\sin\theta} = \frac{a}{\sqrt{\frac{4}{3}(h^2 + k^2 + hk)}}$$

from which we can express

$$a = \frac{\lambda \sqrt{h^2 + k^2 + hk}}{\sqrt{3}\sin\theta} \quad (21)$$

Taking $l=0$ we obtain similarly

$$c = \frac{\lambda l}{2\sin\theta} \quad (22)$$

Using $\lambda=1.5406 \text{ \AA}$ from literature and equations (21) and (22), we obtain the following a values (Figure 26).

2θ	Indices	a [Å]	c [Å]
31.8991	100	3.237	-
34.5872	002	-	5.183
56.7247	110	3.243	-
63.0464	103	-	-
66.5014	200	3.244	-
72.7693	004	-	5.194

Figure 26: ZnO lattice parameters.

The lattice constant values are plotted against functions of θ corresponding to different error variations (Figures 27 to 32), and the y-intercept is the a at 90° . Again, the Nelson-Riley function gives the best fit for lattice constant a . For lattice constant c we have only two points to fit, so we can't conclude which function is the most suitable. We obtain that

$$a = 3.248 \text{ \AA} \quad c = 5.200 \text{ \AA} \quad (23)$$

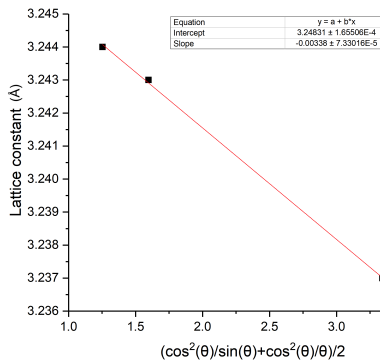


Figure 27: Nelson-Riley function

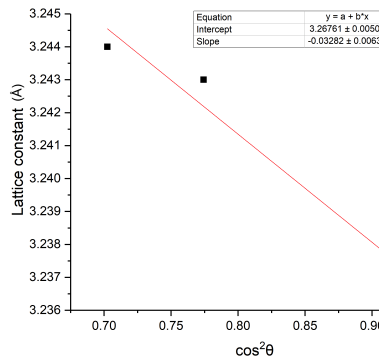


Figure 28: $\cos^2\theta$

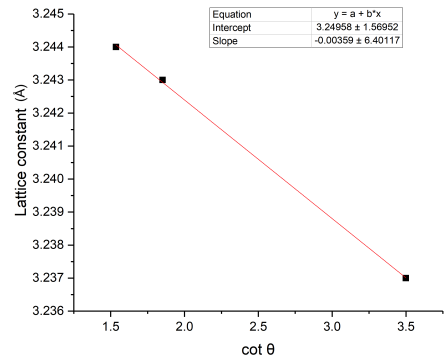


Figure 29: $\cot\theta$

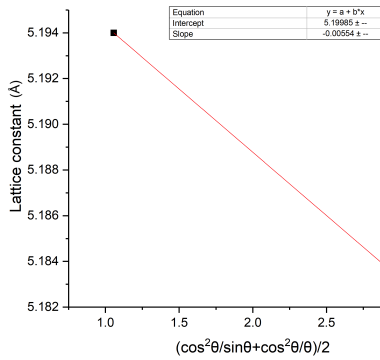


Figure 30: Nelson-Riley function

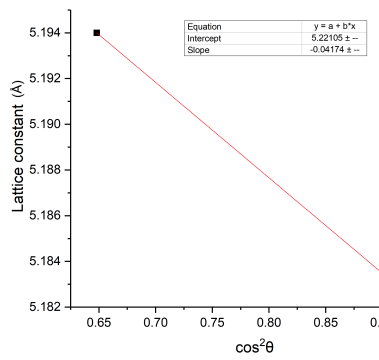


Figure 31: $\cos^2\theta$

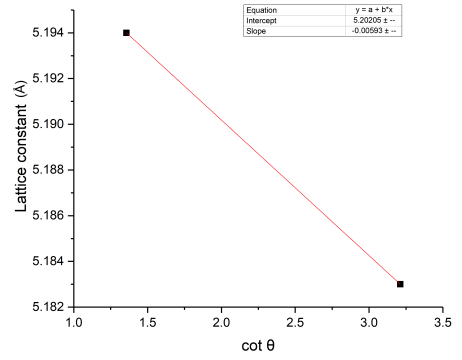


Figure 32: $\cot\theta$

3 Task 2

3.1 Task 2.1

2.1. Measure the XRD patterns ($2\theta - \omega$ scans, 2θ from 20° to 100° , 0.02° , 0.5 sec.) of two different ZnO thin films (about $1\mu\text{m}$ thick) on single-crystalline sapphire substrates with different crystalline orientation of the substrate surface. Sapphire is chemically Al_2O with rhombohedral structure. Consider the given ω -offset values to take into account the miscuts of the sapphire substrates. Note the sample orientation in the diffractometer ("vorn" = this side should show to you).

- (a) ZnO thin film on *a*-plane sapphire (11-20)
- (b) ZnO thin film on *r*-plane sapphire (01-12)

Note: The Millers-Bravais (*hkil*)-notation with four indices corresponds to the usual (*hkl*)notation of the Miller's indices as follows: $i = -(h+k)$ (see Cullity S. 51-52).

- Assign the peaks of ZnO and sapphire using the PC-PDF data base. Use the tool "Spectral lines" in Data Viewer software to identify the weak $\text{Cu K}\beta$ and $\text{W L}\alpha$ peaks.
- Compare the appearance of ZnO $\text{K}\alpha$ -peaks with that of the polycrystalline ZnO sample of task 1. Discuss the structure (orientation, epitaxy) of the ZnO thin films in dependence of the substrate orientation and give the crystallographic growth direction of the two ZnO films.

3.1.1 Different peaks

We have here monocrystalline instead of polycrystalline.

Note after exam: some points got hidden by graphs overlapping

Note after the exam: the blue line is from tungsten because it also gets heated and has radiation and as it's a very heavy element, its L line is around the same range as the K lines for a lighter elements

For assigning the peaks coloured lines are used: pink - $K\beta$, blue - WL_{α_1} , red - K_{α_1} , green - K_{α_2} .

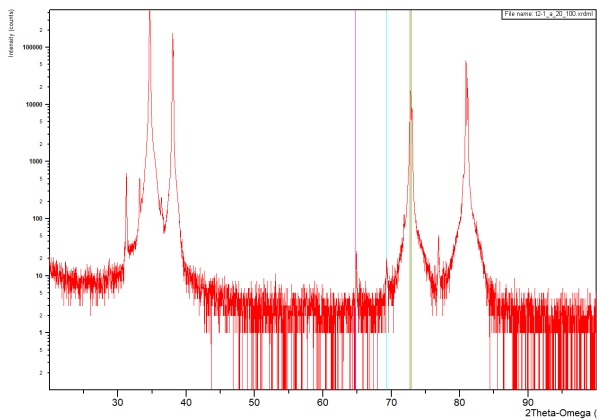


Figure 33: a-plane sapphire peaks

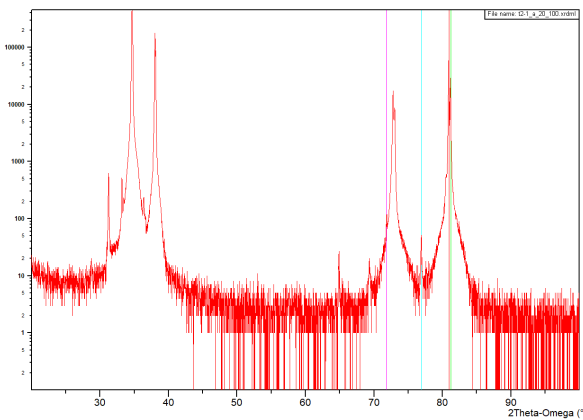


Figure 34: ZnO on a-plane sapphire peaks

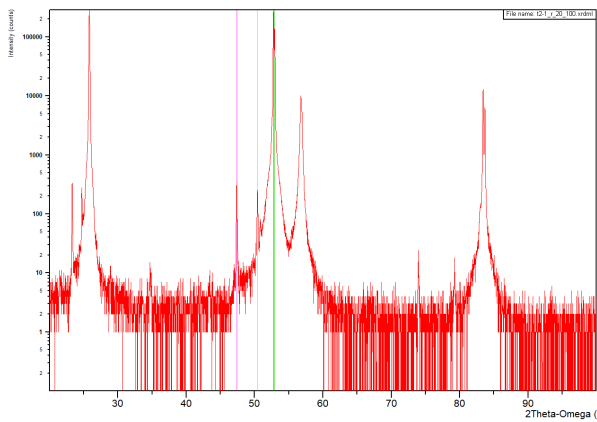


Figure 35: r-plane sapphire peaks

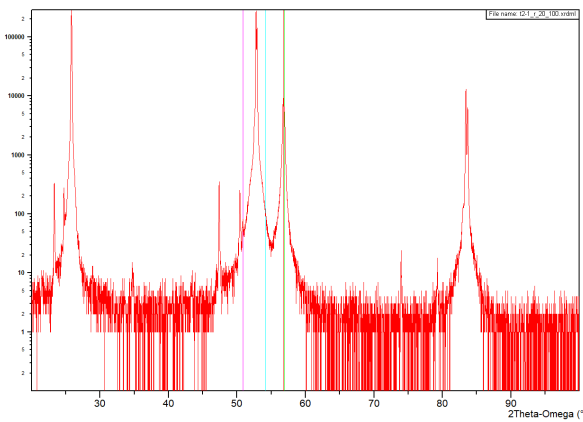


Figure 36: ZnO on r-plane sapphire peaks

For $2\theta - \omega$, the only peaks registered are those from crystallographic planes that are parallel to the surface of the sample. Therefore, for powdered crystalline samples we expect to see more peaks as the grains have different orientations with all possible directions. We see the peaks of any planes in the lattice when the diffraction angle condition is fulfilled. For a thin film we ideally expect only one orientation. The change in the number of peaks can be seen by direct comparison of Figure 22 with Figures 33 to 36. A second difference between polycrystalline (powder) and monocrystalline (thin film) samples is that the peaks for the latter are more intense. This comes from the fact that there is no destructive interference between different indices, since all diffraction comes from the same sets of planes. A third difference is a small broadening of the peaks.

3.2 Task 2.2

Measure for each of the two thin film samples the ZnO and sapphire peaks with the (scan range 5° , step 0.01° , 0.5 sec.) with the detector position fixed at the 2θ position of the selected peak maxima from task No. 2.1.

- Determine by using the Data Viewer software the $K\alpha_1$ peak positions and the full width of half maximum (FWHM) values of the in total four selected $2\theta - \omega$ peaks (two ZnO and two for sapphire) and the four ω -peaks and compare all FWHM values in a table.

- From the $K\alpha_1$ peak positions, calculate the out-of-plane lattice constants c or a of the ZnO thin films perpendicular to the film surface (i.e. out-of-plane) and compare them with that of task 1 and with the PC-PDF values of ZnO.

- The measurements in task 2.2. are the so called ω -scans. They are called in case of use of a high-resolution goniometer "rocking curve". The FWHM of the rocking curves is an important and widely used structural qual-

ity criterion of textured and epitaxial thin films and single crystals. Discuss the FWHMs of the $2\theta - \omega$ peaks (keywords: deviations of lattice plane distance d and coherence length) and ω -scan peaks (keyword: tilt mosaizity) in dependence on the substrate orientation and concerning their relevance for the crystalline sample structure.

3.2.1 Peaks and FWHM

The $2\theta - \omega$ scan peak results, ie the theoretical and measured K_α -peak positions (from figures 33, 34, 35 and 36) as well as the FWHM can be seen in the table below.

a-plane	Theoretical peak position ($^\circ$)	Measured peak position ($^\circ$)	FWHM ($^\circ$)
ZnO(004)	72.516	72.80	0.15
Al ₂ O ₃ (220)	80.664	80.92	0.09
r-plane			
ZnO(110)	56.519	56.8874	0.268
Al ₂ O ₃ (024)	52.533	52.8064	0.085

The ω scans

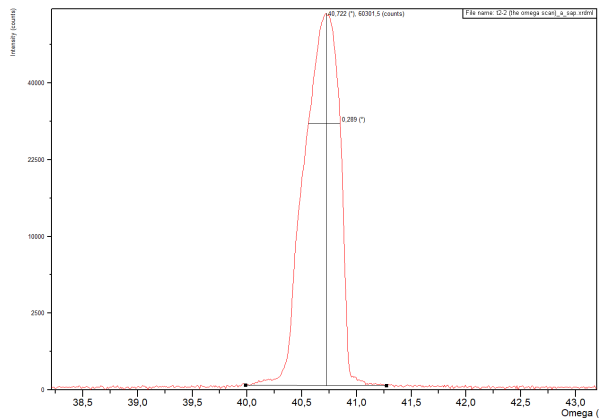


Figure 37: ω scan: a-plane sapphire peaks

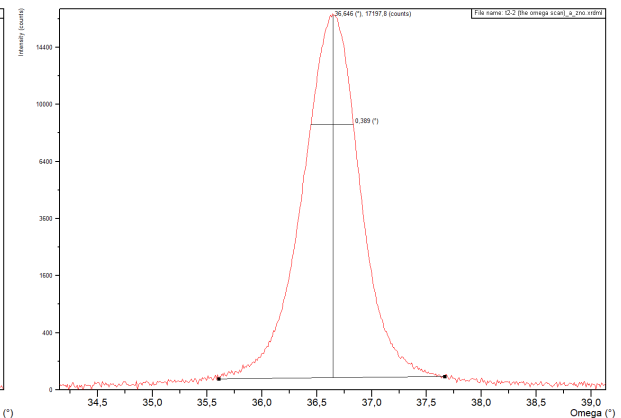


Figure 38: ω scan: ZnO on a-plane sapphire peaks

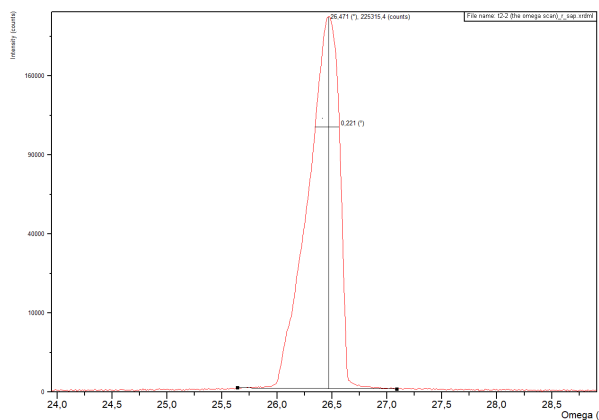


Figure 39: ω scan: r-plane sapphire peaks

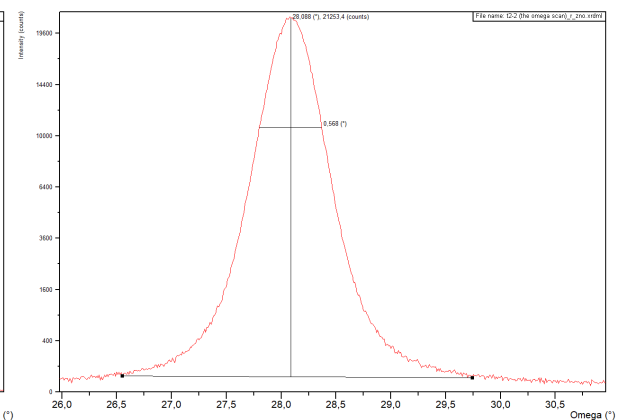


Figure 40: ω scan: ZnO on r-plane sapphire peaks

Results:

a-plane	Measured peak position (°)	FWHM (°)
ZnO(004)	36.646	0.389
Al ₂ O ₃ (220)	40.722	0.289
r-plane		
ZnO(110)	28.088	0.568
Al ₂ O ₃ (024)	26.471	0.221

3.2.2 Lattice constants

Using $\lambda=1.5406 \text{ \AA}$ from literature and equations (21) and (22) from task 1, we obtain the following a values

2θ	Indices	a (Å)	c(Å)
72.80	004	—	5.192
56.8874	110	3.234	—

3.2.3 FWHM discussion

Our peaks for the $2\theta - \omega$ scans were very close to the given theoretical ones. We can conclude some features about the crystal structure from the ω scan.

Compared to an ideal crystal, a mosaic crystal is formed by many crystallites with different angles of inclination $\delta\Omega$ in the [0001] direction (Figure 41). According to the angles $\delta\Omega$, the crystallites can be grouped into ensembles. By rotating the sample around the ω -axis, these different ensembles are detected one after the other. Each of them has a bit different 2θ value. Peaks occur where the Bragg equation $2d_{hkl}\sin(\theta) = n\lambda$ is fulfilled. The 2θ value varies slightly due to mosaicity, so the Bragg equation is fulfilled for slightly different 2θ values. On the graph we can see the broadening of the rocking curve peak. Therefore the width gives us a direct way to see how much the crystals are disoriented around the normal (mean orientation). From this we can conclude that where the FWHM is lower, the crystals are better aligned.

In our sample, for both planes the FWHM value for the thin film is significantly higher than for the substrate. Since the film has grown on the substrate, i.e. the film has adapted to the lattice of the substrate, this is to be expected. The adaptation of the film to the substrate leads to dislocations in the crystal lattice of the film. In our case, only symmetric reflections were measured, thus the FWHM of the ω scans relies on tilt mosaicity. (However, if we measured additionally antisymmetric reflections, twist mosaicity could be seen too.) For r-plane the FWHM of ZnO is significantly higher than for a-plane, suggesting that the lattice mismatch for that plane is bigger than for the a-plane (Figure 42).

Note after the exam: the $2\theta - \omega$ scan peak can get broadened also for very thin films (nanometer scale) because of the finite sample size the destructive interference doesn't happen perfectly at places around the peak. However, in this experiment, the film is thick enough such that this is not the case. Just interesting tho.

Note after the exam: the lattice mismatch between sapphire and ZnO is ca 18.8%, which is very big (good would be 1-2%), so there's no strain because the lattice cannot match (it tries to, but can't), but the crystallites grow with lots of dislocations, which causes the ω peak broadening.

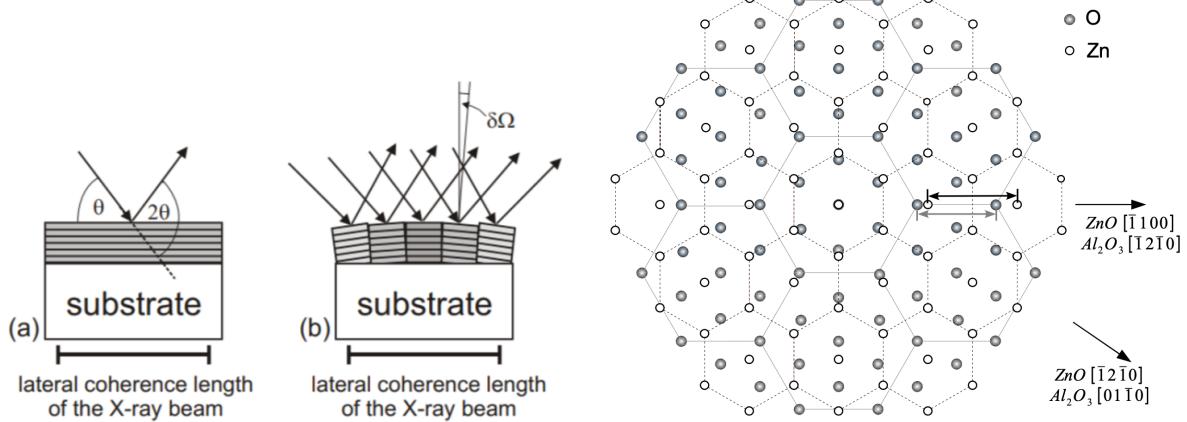


Figure 41: Scheme illustrating the origin of tilt-type dislocations [6]

Figure 42: Scheme illustrating the mismatch between ZnO and sapphire lattices by 30° rotation. For a clearer view only the sapphire O-sublattice and the ZnO Zn-sublattice is depicted. The arrows indicate the distances which are relevant for the calculation of the lattice mismatch [6].

4 Task 3

Prepare and measure a powder sample of an unknown oxide (mention number of the powder bottle) as $2\theta - \omega$ -scan in the range from 10° to 90° in 2θ with step size of 0.02° , and time of 0.5 sec per step.

- Perform a phase analysis using the software X'Pert High Score with implemented PC-PDF data base using an automatic best fit of measured and data base diffraction patterns. You get a table of phase proposals with decreasing score value. Contact the supervisor. Proof the result of the software-based search for different search algorithms related to the different input restrictions (for example without/with consideration of peak intensities).
- Compare and discuss the three best-fit (highest score) search results concerning agreement of peak positions. Discuss crystalline structure and lattice constants of the identified oxide material.

4.1 Diffraction pattern fit

An unknown powder was measured and the diffraction spectrum is shown in 43, above. The spectrum is compared to the PC-PDF data base (Figure 44), the best match is for PbO which occupies all first even places. For comparison, the expected diffraction lines of PbO are shown on Figure 43 below and it quite visible that they match with the measured ones. Therefore we can conclude with certainty that the unknown powder is PbO.

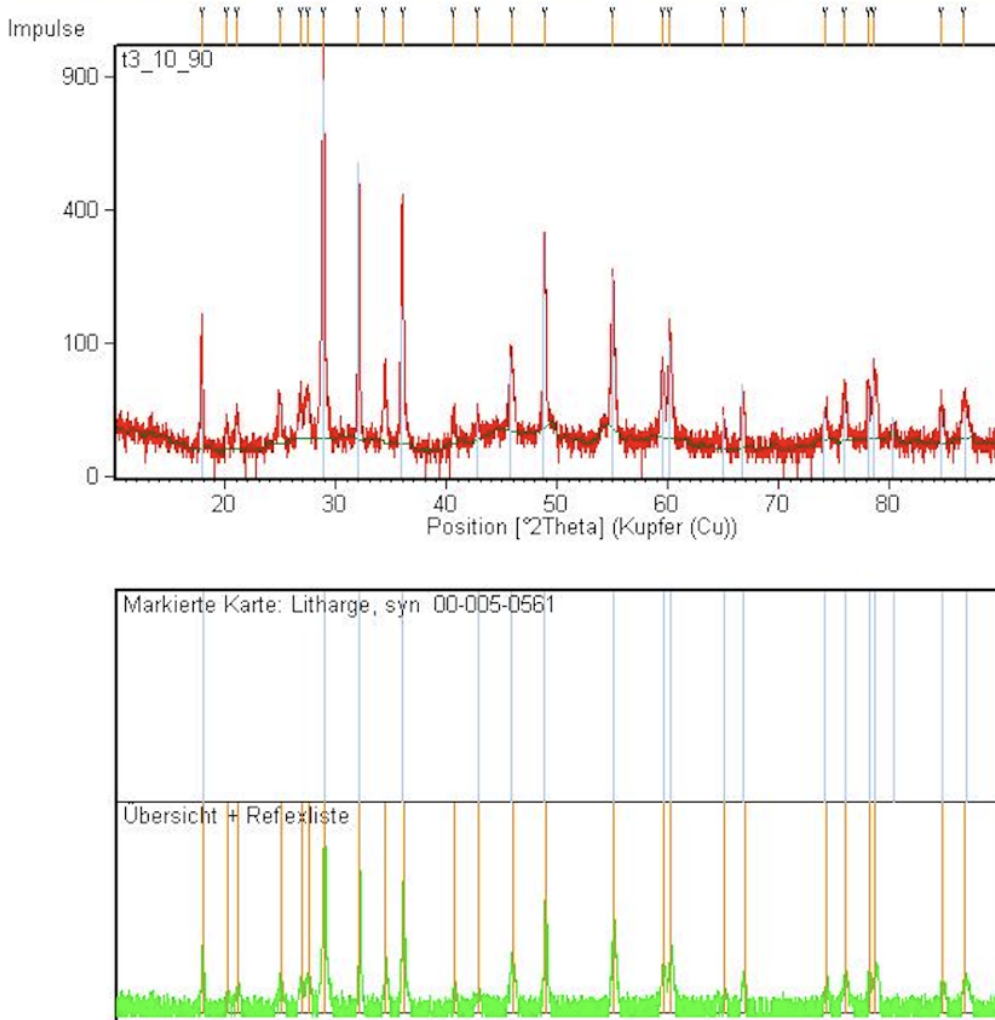


Figure 43: Screenshot from database showing measured peaks vs peaks for PbO

			Litharge, syn	Pb O	
1	00-005-0561				0,842
2	01-078-1666	74	Lead Oxide	Pb O	0,948
3	01-072-0151	62	Massicotite	Pb O	0,589
4	01-078-1665	59	Lead Oxide	Pb O	0,703
5	01-078-1664	54	Lead Oxide	Pb O	0,705
6	00-035-1482	54	Lead Oxide	Pb O	0,514
7	01-078-1663	53	Lead Oxide	Pb O	0,695
8	00-001-0796	40	Litharge	Pb O	0,437
9	01-077-2386	37	Copper Chloride B... (Cu Cl)0.25 (Cu ...		0,278
10	00-026-0856	35	Lithium Silver Bro...	Li0.6 Ag0.4 Br	0,266
11	00-001-0797	34	Litharge	Pb O	0,820

Figure 44: Screenshot from the database showing how well different elements' diffraction patterns match the measured one.

Note after exam: the first compounds after PbO are Copper Chloride etc, which are chemically very different compounds. This clearly illustrates that XRD is a way to look at crystal structure, but not exactly chemical compositions.

4.2 Crystal structure of PbO

PbO occurs in two polymorphs: litharge, having a tetragonal crystal structure, and massicot, having an orthorhombic crystal structure [2].

For the tetragonal case, each Pb atom is bound to four oxygen atoms, forming a square pyramid with a lead atom at the apex. Each oxygen atom is surrounded tetrahedrally by four lead atoms, as can be seen on 45 [7].

Basis vectors:

	Lattice Coordinates	Cartesian Coordinates	Wyckoff Position	Atom Type
\mathbf{B}_1	$\frac{3}{4} \mathbf{a}_1 + \frac{1}{4} \mathbf{a}_2$	$\frac{3}{4} a \hat{\mathbf{x}} + \frac{1}{4} a \hat{\mathbf{y}}$	(2a)	O
\mathbf{B}_2	$\frac{1}{4} \mathbf{a}_1 + \frac{3}{4} \mathbf{a}_2$	$\frac{1}{4} a \hat{\mathbf{x}} + \frac{3}{4} a \hat{\mathbf{y}}$	(2a)	O
\mathbf{B}_3	$\frac{1}{4} \mathbf{a}_1 + \frac{1}{4} \mathbf{a}_2 + z_2 \mathbf{a}_3$	$\frac{1}{4} a \hat{\mathbf{x}} + \frac{1}{4} a \hat{\mathbf{y}} + z_2 c \hat{\mathbf{z}}$	(2c)	Pb
\mathbf{B}_4	$\frac{3}{4} \mathbf{a}_1 + \frac{3}{4} \mathbf{a}_2 - z_2 \mathbf{a}_3$	$\frac{3}{4} a \hat{\mathbf{x}} + \frac{3}{4} a \hat{\mathbf{y}} - z_2 c \hat{\mathbf{z}}$	(2c)	Pb

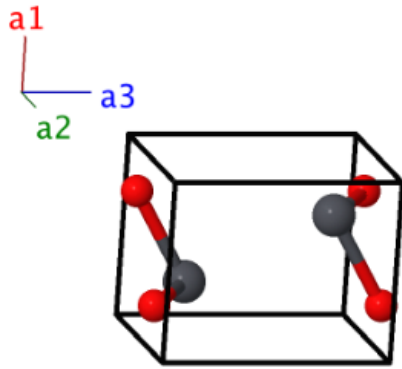


Figure 45: The unit cell of tetragonal PbO [8]

5 Summary

In this experiment, X-ray diffraction was used to investigate several materials with crystalline structure. In the first task, powdered samples of Si and ZnO were examined. As they were powdered, the orientations of separate grains were distributed over all possible directions. Based on information from a database, different peaks of the X-ray diffraction patterns were assigned with their corresponding Miller's indices. Using the X'Pert High Score software, a list of exact peak locations and the corresponding d -values were generated. From the latter, lattice parameters can be calculated, taking into account the geometry of the unit cell structure for each compound. Using the Nelson-Riley function for correcting the error the following lattice constants were found:

- Si: $a = 5.432 \text{ \AA}$
- ZnO: $a = 2.248 \text{ \AA}$, $c = 5.200 \text{ \AA}$

In the second task, thin films of the same compounds (Si and ZnO) were used. This produced far less X-ray diffraction pattern peaks, but with higher amplitude. The FWHM of the $2\theta - \omega$ scan and ω scan were discussed and it was seen that the thin film peaks' FWHM was significantly higher than for the substrate, which makes sense, since the thin film lattice had to adapt to the substrate lattice: the mismatch of the lattice constants produces dislocations in the thin film.

In the third task, an unknown powder was examined and, comparing the obtained X-ray diffraction peaks to the database, it was found to be PbO.

References

- [1] M. Alonso and E.J. Finn. *Physics*. Addison-Wesley series in physics. Addison-Wesley, 1970. ISBN: 9780201002409. URL: <https://books.google.de/books?id=LS4bAQAAIAAJ>.
- [2] Dodd S. Carr. “Lead Compounds”. In: *Ullmann's Encyclopedia of Industrial Chemistry* (2005). DOI: [10.1002/14356007.a15_249](https://doi.org/10.1002/14356007.a15_249).
- [3] B.D. Cullity, S.R. Stock, and S.R. Stock. *Elements of X-ray Diffraction*. Addison-Wesley series in metallurgy and materials. Prentice Hall, 2001. ISBN: 9780201610918. URL: <https://books.google.de/books?id=IiXwAAAAMAAJ>.
- [4] W. Demtröder. *Atoms, Molecules and Photons: An Introduction to Atomic-, Molecular- and Quantum Physics*. Graduate Texts in Physics. Springer Berlin Heidelberg, 2019. ISBN: 9783662555217. URL: <https://books.google.de/books?id=HOTvswEACAAJ>.
- [5] H. Haken, W.D. Brewer, and H.C. Wolf. *The Physics of Atoms and Quanta: Introduction to Experiments and Theory*. Advanced Texts in Physics. Springer Berlin Heidelberg, 2006. ISBN: 9783540292814. URL: <https://books.google.de/books?id=uZ9bcSqcSVsC>.
- [6] Walter Schottky Institut und Zentralinstitut der Technischen Universität München für physikalische Grundlagen der Halbleiterelektronik. “Fortgeschrittenpraktikum: High Resolution X-Ray Diffraction”. In: (Sept. 2007).
- [7] J. Leciejewicz. “On the crystal structure of tetragonal (red) PbO”. In: *Acta Crystallographica* (1961). DOI: [10.1107/S0365110X61003892](https://doi.org/10.1107/S0365110X61003892).
- [8] J. Leciejewicz. “The AFLOW Library of Crystallographic Prototypes: Part I”. In: *Computational Materials Science* (May 2017). DOI: [10.1016/j.commatsci.2017.01.017](https://doi.org/10.1016/j.commatsci.2017.01.017).
- [9] H.G.J. Moseley. “The high frequency spectra of the elements. Part II”. In: *Phil. Mag* 6. 27 (1914), pp. 703–713. URL: <https://archive.org/details/londonedinburg6271914lond/page/712/mode/2up>.
- [10] K. Razi Naqvi. “The physical (in)significance of Moseley’s screening parameter”. In: *American Journal of Physics* 64.10 (Oct. 1996), pp. 1332–1332. DOI: [10.1119/1.18381](https://doi.org/10.1119/1.18381). URL: <https://doi.org/10.1119/1.18381>.
- [11] Ü. Özgür et al. “A comprehensive review of ZnO materials and devices”. In: *Journal of Applied Physics* 98.4 (Aug. 2005), p. 041301. DOI: [10.1063/1.1992666](https://doi.org/10.1063/1.1992666). URL: <https://doi.org/10.1063/1.1992666>.
- [12] L. Spieß et al. *Moderne Röntgenbeugung: Röntgendiffraktometrie für Materialwissenschaftler, Physiker und Chemiker*. Springer Fachmedien Wiesbaden, 2019. ISBN: 9783834882325. URL: <https://books.google.de/books?id=DJqRDwAAQBAJ>.
- [13] James T. Yardley. “Silicon Basics - General Overview”. In: (2001). URL: <https://www1.columbia.edu/sec/itc/ee/test2/pdf%20files/silicon%20basics.pdf>.